

# High-concentration silver alloying and steep back-contact gallium grading enabling copper indium gallium selenide solar cell with 23.6% efficiency

Received: 31 August 2023

Accepted: 26 January 2024

Published online: 19 February 2024

Check for updates

Jan Keller<sup>1</sup>✉, Klara Kiselman<sup>1</sup>, Olivier Donzel-Gargand<sup>1</sup>,  
Natalia M. Martin<sup>1</sup>, Melike Babucci<sup>1</sup>, Olle Lundberg<sup>2</sup>, Erik Wallin<sup>2</sup>,  
Lars Stolt<sup>1</sup> & Marika Edoff<sup>1</sup>

Chalcopyrite-based solar cells have reached an efficiency of 23.35%, yet further improvements have been challenging. Here we present a 23.64% certified efficiency for a (Ag,Cu)(In,Ga)Se<sub>2</sub> solar cell, achieved through the implementation of a series of strategies. We introduce a relatively high amount of silver ( $[Ag]/([Ag] + [Cu]) = 0.19$ ) into the absorber and implement a ‘hockey stick’-like gallium profile with a high concentration of Ga close to the molybdenum back contact and a lower, constant concentration in the region closer to the CdS buffer layer. This kind of elemental profile minimizes lateral and in-depth bandgap fluctuations, reducing losses in open-circuit voltage. In addition, the resulting bandgap energy is close to the local optimum of 1.15 eV. We apply a RbF post-deposition treatment that leads to the formation of a Rb–In–Se phase, probably RbInSe<sub>2</sub>, passivating the absorber surface. Finally, we discuss future research directions to reach 25% efficiency.

About a decade ago, the implementation of heavy alkali elements into the absorber film and at its interfaces initiated a gradual increase in efficiency ( $\eta$ ) of chalcopyrite-based solar cells from about 20% to 23% (refs. 1–4). More recently, the addition of silver to Cu(In,Ga)Se<sub>2</sub> (CIGS) was found to facilitate grain growth by lowering the absorber melting temperature and enhancing reaction rates during phase evolution<sup>5–8</sup>. Silver partially replaces copper in the chalcopyrite lattice, forming (Ag,Cu)(In,Ga)Se<sub>2</sub> (ACIGS) films. Moreover, Ag alloying is suggested to reduce the structural disorder<sup>9</sup>, ease interdiffusion of Ga and In during deposition<sup>8</sup>, lower the energetic positions of the conduction and valence band edges<sup>10–12</sup> and allow for more close-stoichiometric absorber compositions without shunting issues<sup>13</sup>.

A record efficiency of 23.35% was reached by Solar Frontier (SF) in 2019, using the sequential sulfurization after selenization of

metallic precursors to fabricate the (Ag,Cu)(In,Ga)(S,Se)<sub>2</sub> absorber film (amount of Ag <1 at.%)<sup>2,13</sup>. This approach usually leads to a constant  $[Ga]/([Ga] + [In])$  (GGI) in the upper half of the absorber and an increasing GGI towards the Mo back contact. The resulting back surface field, created by a gradient in electron affinity, enhances carrier collection and reduces the back-contact recombination rate<sup>14</sup>. To mitigate recombination in the space charge region (SCR) and at the interface to the buffer layer, SF added sulfur at the very surface of the absorber. The resulting gradual decrease in the valence band minimum and increase in bandgap energy ( $E_g$ ) towards the buffer layer reduce the hole concentration at the heterojunction and lead to an increase in open circuit voltage ( $V_{oc}$ )<sup>15</sup>.

When the absorber is deposited via the multi-stage co-evaporation method, sulfur is usually not added. To minimize the recombination at

<sup>1</sup>Department of Material Science and Engineering, Division of Solar Cell Technology, Ångström laboratory, Uppsala University, Uppsala, Sweden.

<sup>2</sup>Evoler AB (now First Solar European Technology Center AB), Uppsala, Sweden. ✉e-mail: [jan.keller@angstrom.uu.se](mailto:jan.keller@angstrom.uu.se)

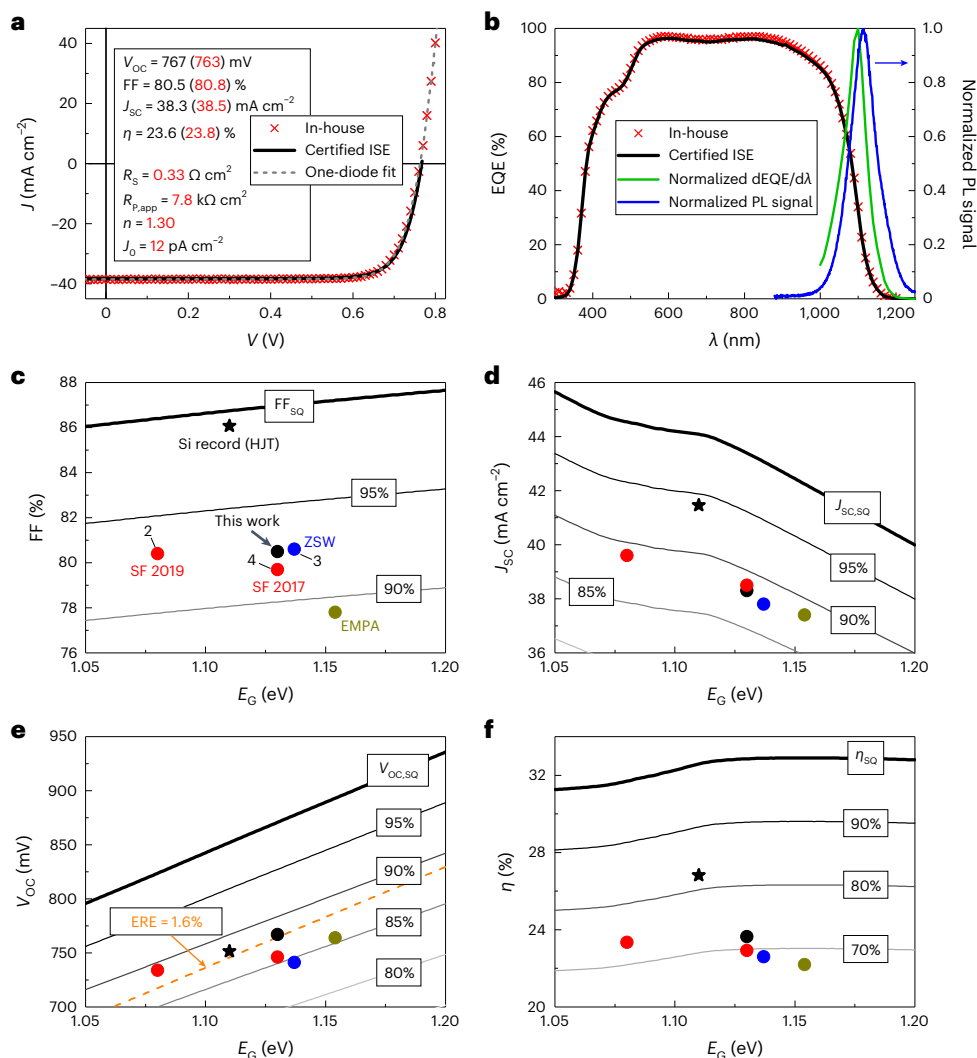


**Fig. 1 | Solar cell characteristics and parameter comparison.** **a, b**, Current–voltage characteristics (**a**) and EQE spectra (**b**) obtained from in-house measurements as well as externally calibrated and independently certified by Fraunhofer ISE. The inset in **a** lists the JV (black, certified; red, in-house) and diode parameters as extracted from a one-diode fit to the in-house measurement. The wider voltage range allows for a more accurate determination of the series resistance ( $R_s$ ). The other diode parameters are the apparent parallel resistance ( $R_{p,app}$ ), the dark saturation current density ( $J_0$ ) and the ideality factor ( $n$ ). In **b** the normalized PL and first derivative of the EQE are added, too. **c–f**, The solar

cell parameters FF (**c**),  $J_{sc}$  (**d**),  $V_{oc}$  (**e**) and  $\eta$  (**f**) of our device as a function of the respective bandgap energy (from  $dEQE/dE$ ) are compared with literature data (see Table 1 for details). For comparison, the parameters of a state-of-the-art Si heterojunction solar cell (HJT) are added, too<sup>37</sup>. Different percentages of the theoretical maximum values in the radiative limit as a function of the bandgap are plotted as solid lines. In **e**, the predicted  $V_{oc}$  trend for an ERE of 1.6%, as measured for the record device presented in this work, is shown by the dashed curve (derived from equation (1)).

the interfaces and enhance carrier collection, a ‘notch’ (sometimes also ‘V-shaped’) GGI profile, with lowest GGI close to the SCR edge, is commonly implemented<sup>16–20</sup>. Using a three-stage co-evaporation method and a GGI ‘notch’ profile,  $\eta = 22.6\%$  was reached in 2016 by the Zentrum für Sonnenenergie- und Wasserstoff-Forschung (ZSW)<sup>3</sup>.

In this Article, we report a 23.64% certified efficiency. Instead of a notch profile, we implement a ‘hockey stick’-like GGI profile, with a rather constant Ga content in the upper half of the absorber and a strongly increased concentration close to the back contact. This minimizes lateral and in-depth bandgap fluctuations, potentially resulting in reduced  $V_{oc}$  losses<sup>21,22</sup>. Additionally, we incorporate a relatively high silver amount of  $[Ag]/([Ag] + [Cu])$  (AAC) = 0.19 into the absorber. We apply a standard RbF post-deposition treatment (PDT), allowing to reduce the thickness of the CdS buffer layer to 25 nm. Finally, we observe that extensive light soaking maximizes the efficiency

(saturating  $V_{oc}$  and fill factor (FF)), as previously reported for CIGS devices subjected to heavy alkali PDTs<sup>23,24</sup>.

We conclude with a discussion of remaining limitations and possible ways to improve the efficiency towards 25%.

## Results

### Electro-optical characterization of the champion device

Figure 1a shows the current-density versus voltage ( $J$ – $V$ ) characteristics of the champion cell measured in-house ( $\eta = 23.75\%$ ) and certified by Fraunhofer Institute for Solar Energy Systems (ISE) ( $\eta = 23.64\%$ ). The ideality factor of  $n = 1.30$  is lower than previously reported values for high-efficiency solar cells with  $\eta = 22.9\%$  ( $n = 1.38$ )<sup>4</sup> and  $\eta = 22.6\%$  ( $n = 1.39$ )<sup>3</sup>. This indicates that the overall recombination rate in the SCR is reduced, either due to a lower activation energy or a lower density of the dominant defect(s) in the SCR ( $n = 2$  would mean dominant

**Table 1 | PV parameters of state-of-the-art (A)CIGS solar cells from the literature**

	$V_{oc}$ (mV)	$J_{sc}$ (mAcm <sup>-2</sup> )	FF (%)	$\eta$ (%)	$E_g$ (eV) from dEQE/dE	(First) Buffer	Heavy alkali	Ag addition
EMPA <sup>a</sup>	764	37.4	77.8	22.19	1.154	CdS	RbF	Yes (AAC=0.02)
ZSW	741	37.8	80.6	22.6	1.137	CdS	RbF	No
SF 2017	746	38.5	79.7	22.92	1.13	CdS	CsF	No
SF 2019	734	39.6	80.4	23.35	1.08	Zn(O,S)	CsF	Yes (AAC<0.04)
This work	767	38.3	80.5	23.64	1.130	CdS	RbF	Yes (AAC=0.19)

<sup>a</sup>EMPA record device does not use glass substrate, but flexible polymer foil. Externally certified solar cell parameters of the best devices from other research institutes<sup>2–4</sup>. EMPA data were kindly provided through personal communication with R. Carron;  $E_g$  values for the ZSW data were kindly provided through personal communication with W. Witte. The respective  $E_g$  values (all from dEQE/dE), used buffer layers in contact to the absorbers (sometimes multiple buffers were implemented), types of heavy alkali PDT and whether Ag was alloyed to the absorber are also listed.

recombination via mid-gap defects in SCR, while interface recombination is less of an issue for state-of-the-art devices)<sup>25,26</sup>.

Figure 1b illustrates the corresponding external quantum efficiency (EQE) spectra measured on the entire cell/aperture area, so that constant shading losses of about 1.2% by the metal grid fingers are included. In the wavelength ( $\lambda$ ) range from 550 to 850 nm, internal collection losses are negligible and the remaining losses are exclusively caused by the cell reflection, which is reduced to <3% thanks to the application of a MgF<sub>2</sub> anti-reflection coating. For lower  $\lambda$  values, parasitic absorption in the CdS buffer and, to a minor extent, in the window layer stack reduces the EQE. From fitting the EQE spectrum (Supplementary Fig. 1) it can be estimated that the total  $J_{sc}$  loss is about 1.4 mA cm<sup>-2</sup> by parasitic absorption in the CdS ( $E_{G,CdS}$  = 2.4 eV) and at least 0.8 mA cm<sup>-2</sup> in the i-ZnO/ZnO:Al window layer stack ( $E_{G,ZnO}$  = 3.3–3.4 eV). Thus, the potential to increase the short-circuit current density ( $J_{sc}$ ) by using alternative buffers and window layers with higher  $E_g$  is still quite large for this record solar cell (estimated efficiency without parasitic absorption is 25.0%). In fact, parasitic absorption could be almost completely avoided for  $E < 3.45$  eV for the best solar cells made by SF with very thin (few nanometres) CdS or high bandgap Zn(O,S) buffer layers<sup>2</sup>. Ultimately, solid phase crystallized In<sub>2</sub>O<sub>3</sub>:H may be used as a transparent conductive oxide to essentially avoid any parasitic absorption in the window layer<sup>27,28</sup>.

For  $\lambda > 850$  nm, the EQE level decreases due to incomplete absorption, carrier collection losses and, to a minor extent, free carrier absorption in the transparent conductive oxide until  $E_g$  is reached. One way to extract the bandgap from the EQE spectrum is to identify the energy of the maximum of the first derivative (dEQE/dE or dEQE/d $\lambda$ ). The corresponding normalized dEQE/d $\lambda$  curve of the certified measurement is added in Fig. 1b and gives  $E_g$  = 1.130 eV. Moreover, the spectral photoluminescence (PL) yield was measured at room temperature in a region just outside the active cell area after selectively removing the window layer stack. The respective PL spectrum is added in Fig. 1b as well. Taking the peak energy as a measure of the bandgap leads to a slightly lower value of  $E_g$  = 1.114 eV. An Urbach energy ( $E_U$ ) of 14.5 meV was extracted from the EQE spectrum, which is a typical value for highly efficient chalcopyrite solar cells<sup>29–31</sup>. The fit is presented together with a clearer illustration of the PL spectrum in Supplementary Fig. 2. It should be mentioned that the  $E_U$  derived from EQE appears to be an overestimation and the extraction from PL gives slightly lower values<sup>31,32</sup>.

Table 1 summarizes the JV parameters of the best chalcopyrite-based solar cells from different research institutes (all externally certified and data taken from refs. 2–4,  $E_g$  values for the Eidgenössische Materialprüfungs- und Forschungsanstalt (EMPA) and ZSW devices from private communication). All corresponding absorbers were subjected to a heavy alkali PDT, and for the two highest efficiencies Ag was alloyed as well. Silver was also added by EMPA to achieve a remarkable value of  $\eta$  = 22.2% for a flexible ACIGS solar cell, using a polymer substrate and thus requiring lower growth temperatures.

Figure 1c–f plots the JV parameters from Table 1 as a function of the corresponding bandgap energies and sets them in perspective to the respective maximum values in the radiative SQ limits<sup>33</sup>. All solar cells show quite similar losses in  $J_{sc}$  of 11–12%. Except for the EMPA device that was processed at a lower temperature, all samples exhibit rather low relative FF losses  $\leq 8\%$ . The lowest  $V_{oc}$  deficit (11%) was reached for the SF sample with  $\eta$  = 23.35%, slightly better than the record device presented in this work (12% loss). Thus, both  $J_{sc}$  and  $V_{oc}$  of the best chalcopyrite-based solar cells show the same potential (greater than FF) for efficiency improvements.

The experimental  $V_{oc}$  is a measure of the quasi Fermi level splitting (divided by the elemental charge  $e$ ), and consequentially the following equation should apply when substantial interface recombination can be excluded<sup>34,35</sup>:

$$V_{oc,exp} = V_{oc,SQ} + \frac{kT}{e} \ln(ERE) \quad (1)$$

with  $k$  and  $T$  being the Boltzmann constant and the temperature, respectively. The term  $\frac{kT}{e} \ln(ERE)$  is a measure of the non-radiative recombination losses and includes the external radiative efficiency (ERE), which is the ratio of the emitted to the absorbed photon flux. For the champion device, a value of 1.6% was measured at 1 sun illumination intensity after 7 h of light soaking, being (to the best of our knowledge) the highest ever reported ERE for a chalcopyrite absorber (at least when measured directly from PL and not indirectly derived from  $V_{oc}$  and the EQE as in ref. 36). The measurements can be found in Supplementary Fig. 3. The theoretical  $V_{oc}$  trend for ERE of 1.6% (as derived from equation (1)) is shown by the orange dashed curve in Fig. 1e. Obviously, the measured  $V_{oc}$  (767 mV) is in good agreement with the one predicted by the ERE value of 765 mV (but would deviate more if  $E_g$  was taken from PL peak,  $E_g$  = 1.114 eV).

For comparison, the parameters of the record Si heterojunction solar cell with  $\eta$  = 26.8% are added in Fig. 1c–f as well<sup>37</sup>. The  $V_{oc}$  deficits of the best chalcopyrite devices are on par with the best Si solar cell (that is, also the ERE<sup>36</sup>). However, much lower FF and  $J_{sc}$  losses were achieved for the Si record cell.

Finally, the efficiency of the presented champion device reaches 72.0% of the SQ limit for the corresponding bandgap energy, which is lower than for the best cell from SF (73.7%). Thus, the reason for setting the new record efficiency is probably not a superior absorber quality or cell design, but rather that we were able to fabricate a very high-quality absorber with a higher bandgap energy that better matches the AM1.5G spectrum than the SF 2019 record device.

### Microscopic characterization of the complete device stack

As shown in the scanning electron microscopy (SEM) images in Fig. 2a,b, large ACIGS grains are formed, with most of them being sized >1  $\mu$ m in all dimensions. The topography is not particularly smooth, but rather rough. The resulting tilted light in-coupling after refraction at the CdS/

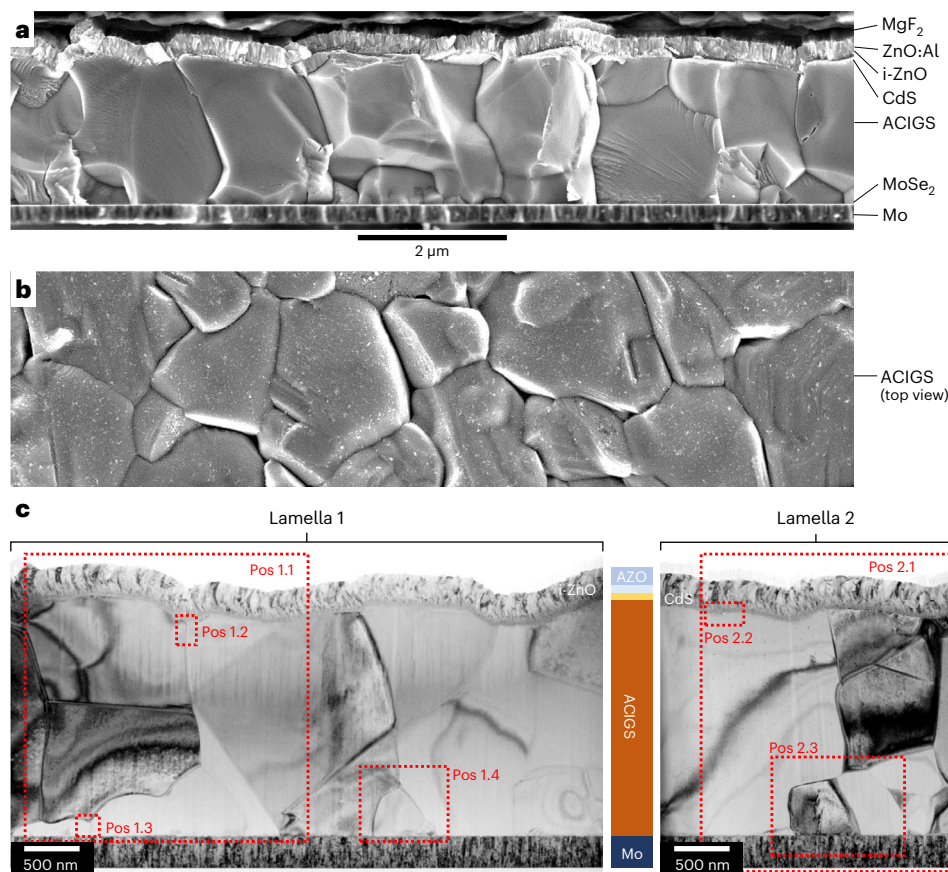


**Fig. 2 | Electron microscopy analysis of the device structure.** **a, b,** SEM images of the full cross-section of the complete champion cell (**a**) and the absorber surface after selectively removing the CdS and window layers via HCl etching (**b**). The 2  $\mu\text{m}$  scale bar refers to both panels **a** and **b**. **c,** BF-TEM images of the full cross-sections of the solar cell for the two lamellae investigated. The areas

for which the elemental distribution was analysed by scanning (S)TEM-EDS are highlighted with red boxes ('Pos1.x', lamella 1; 'Pos2.x', lamella 2). A schematic of the solar cell cross-section is illustrated between the two lamellae. The ZnO:Al film is abbreviated as AZO.

ACIGS interface is beneficial, since it increases the optical path length in the absorber.

To obtain a higher-resolved analysis of the absorber and interface structures, we prepared two thin (<100 nm) cross-section lamellae of the full cell stack via a focused-ion beam (FIB). Figure. 2c shows the bright-field (BF) transmission electron microscopy (TEM) images of those two lamellae. The red dashed rectangles show the positions that were analysed by energy-dispersive X-ray spectroscopy (EDS), providing elemental distribution maps, which are illustrated either later in the manuscript or in Supplementary Information.

Lamella 1 was further studied on a nano-scale by X-ray fluorescence spectroscopy (nano-XRF). The measured relative elemental distributions of the absorber metal elements and Rubidium are displayed in Fig. 3. Semi-transparent Ga and Rb distribution maps, superimposed on the TEM image, can be found in Supplementary Fig. 4. In addition to the nano-XRF results, the elemental maps from 'Pos1.I', as obtained via EDS in scanning TEM (STEM) mode, are shown in Fig. 3 for comparison. A more detailed presentation of these STEM-EDS results at 'Pos1.I' can be found in Supplementary Fig. 5.

First, we observed that the nano-XRF and STEM-EDS experiments provide similar results regarding the absorber metal distribution. The exception is the Ag signal, which is too low in the case of the nano-XRF analysis to obtain reliable information, due to the superposition of the L edges of Ag, In and Cd. As intended, the upper half of the absorber exhibits a rather constant GGI level with only minor lateral variations, indicating only small  $E_c$  fluctuations at the surface and in the SCR<sup>21,22</sup>.

Bandgap fluctuations may further arise from spatial variations in stress or stoichiometry<sup>21</sup>. However, the observed minor compositional variations, together with the large ACIGS grain size, indicate moderate lattice stress (which may be larger in the direct vicinity of the CdS layer though). Moreover, the stoichiometry is found to be rather constant in the top half of the absorber ( $([\text{Ag}] + [\text{Cu}]) / ([\text{Ga}] + [\text{In}]) = [\text{I}]/[\text{III}] \approx 0.83$ ). A steep increase in GGI towards the Mo electrode is observed in the bottom third of the ACIGS, which should effectively repel electrons from the back contact. While suffering from a lower spatial resolution, an advantage of the nano-XRF method over STEM-EDS is the higher sensitivity to heavy alkali elements<sup>38–40</sup>. It can be clearly seen that Rb agglomerates consistently (that is, no gaps) at the interfaces with CdS at the front and with MoSe<sub>2</sub> at the back contact. Furthermore, it is found in certain grain boundaries (GBs), while others are Rb free. This feature was detected in previous studies where it was shown that heavy alkali atoms such as Rb and Cs do not diffuse into high-symmetry twin boundaries, but only decorate random high-angle GBs<sup>38–40</sup>.

The highest Rb concentration is found in isolated patches at the ACIGS/CdS heterojunction. Similar patches were reported in earlier studies for absorbers subjected to a CsF-PDT and suggested to indicate the formation of a Cs(In,Ga)Se<sub>2</sub> phase<sup>39</sup>. We provide a more detailed description of the Rb-containing patches later in the manuscript.

Even after 10 years of research, it is still under debate which effect(s) are responsible for the performance improvement by the heavy alkali PDT. Discussed mechanisms are a reduced GB band

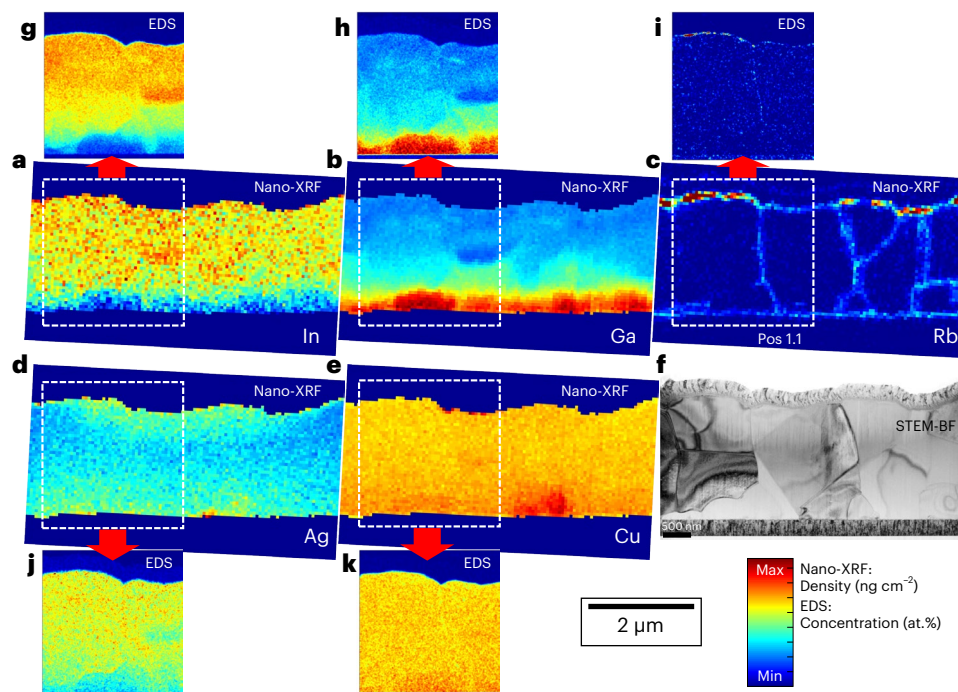


**Fig. 3 | Nano-XRF and STEM-EDS analysis of lamella 1.** **a–e**, Elemental distribution of the absorber metals In (**a**), Ga (**b**), Ag (**d**), Cu (**e**) and Rb (**c**), as obtained via nano-XRF on lamella 1 from Fig. 2c. XRF peak fitting was conducted by using the dedicated software PyMca<sup>66</sup>. To account for the small thickness variations across the lamella (XRF intensity/scales with sample volume), the signal intensity of the absorber metal elements was corrected at each pixel (that is, position) by multiplying it with an individual correction factor  $m_{\text{cor}}(\text{pixel}) = I_{\text{Se,Max}}/I_{\text{Se}}(\text{pixel})$  obtained from the Se distribution map. Here,  $I_{\text{Se,Max}}$  is the highest intensity of the Se map and  $I_{\text{Se}}(\text{pixel})$  is the intensity measured at each

corresponding pixel. This is a valid first approximation as long as the selenium concentration can be assumed to be constant everywhere in the absorber (that is, 1:1:2 stoichiometry). Consequently, the Se distribution map is not shown. **f**, Corresponding STEM-BF image. **g–k**, Corresponding maps of a smaller area ('Pos1.1', indicated by a dashed white box) derived from STEM-EDS for In (**g**), Ga (**h**), Rb (**i**), Ag (**j**) and Cu (**k**). The colour code refers to the atomic concentrations in at.% in case of the EDS analysis and to the density (in  $\text{ng cm}^{-2}$ ) in case of the nano-XRF analysis, ranging from the corresponding minimum (Min) to the maximum (Max) values. The scale bar is valid for all images.

bending, lower Urbach energy, increased p-type doping and the formation of a wide-gap alkali–In–Se surface phase<sup>31,41</sup>.

Figure 4 displays the elemental maps of Rb, In and Ga at four different absorber positions, as measured by nano-XRF of the bare absorber films (top view) after removing the window and buffer layers (compare Fig. 3b). We observe a clear anti-correlation between the Ga and In concentrations. This is not related to GGI fluctuations at the surface but illustrates the different depth at which the GGI suddenly increases towards the back contact (XRF signal stems from entire absorber volume). Rubidium seemingly agglomerates at GBs and its distribution is interrupted in places, indicating the presence of twin boundaries at the absorber surface. At some positions, the Rb signal is notably higher, suggesting the presence of the Rb-rich patches observed in the cross-section in Fig. 3. However, it cannot be excluded that those patches were selectively removed by the HCl etch, as proposed in earlier studies for alkali–In–Se surface phases<sup>42–44</sup>. The weaker Rb signal from the grain interior most probably originates from the back interface as well as from tilted and deeper GBs.

To investigate the Rb-rich patches in more detail and provide a quantification of the elemental depth-profiles, the positions 'Pos2.1' and 'Pos2.2' on lamella 2 were thoroughly analysed via STEM-EDS and the results are discussed in the following. The distribution of all absorber elements and Rb at 'Pos2.1' are shown in Fig. 5.

As seen for lamella 1, the upper half of the absorber shows a rather constant GGI and AAC (that is, also constant  $E_g$ ). We extracted a line scan along the arrow drawn inside the Ga map. We did the same for 'Pos1.1' of lamella 1 (Supplementary Fig. 5) and quantified the average surface composition as  $\text{GGI} \approx \text{AAC} \approx 0.25$  from STEM-EDS. The region with only minor compositional fluctuations in the upper part

of the absorber is more extended in lamella 1 (compare Supplementary Fig. 5). Generally, STEM-EDS analysis provides limited statistics about lateral differences in composition and microstructure, due to the small extracted sample volume and the time- and work-intensive nature of the technique. In the lower part of the ACIGS layer the GGI increases, while the AAC decreases. The reduced Ag content in regions of higher Ga concentration was observed in prior studies and can be explained by a thermodynamically driven, composition-dependent instability of the ACIGS system<sup>45</sup>. The GGI at the back contact reaches a value close to 0.7 here, but deviates laterally (for example, GGI of 0.8 in Supplementary Fig. 5). Overall, the GGI at the  $\text{MoSe}_2/\text{ACIGS}$  interface ranges between 0.65 and 0.80 for all investigated locations.

To obtain a quantified average composition profile, glow-discharge optical emission spectroscopy was measured on the same sample. The results are illustrated together with the normalized intensities of Cd, Mo, Rb and Na (Na peaks at Mo/glass interface) in Supplementary Fig. 6. The obtained GGI and AAC profiles are very similar to the ones deduced from STEM-EDS. However, the surface GGI and AAC are slightly lower when extracted via GDOES, which may be an artefact of the destructive nature of the technique (for example, smearing out of interfaces). The bandgap value extracted from EQE can be used to calculate an estimation of the surface composition<sup>10</sup>, since the Ga content is lowest at the buffer interface. For  $E_g = 1.13$  eV a value of GGI of  $-0.23$  is deduced, assuming AAC of 0.20, which is closer to the surface composition derived from STEM-EDS.

As discussed previously, rubidium is mainly concentrated in patches ( $<100$  nm in size) beneath the CdS layer, but smaller amounts can be found everywhere at the ACIGS/CdS interface (Fig. 3). Both profiles (EDS in Fig. 5b and GDOES in Supplementary Fig. 6) show that the Rb signal peaks just

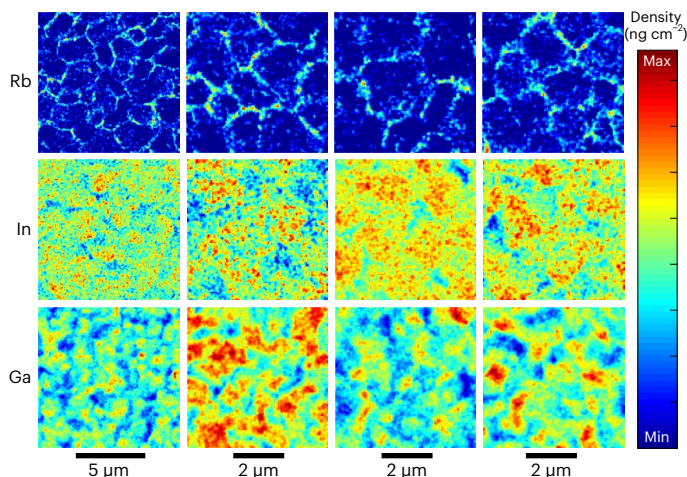


**Fig. 4 | Lateral distribution of rubidium, indium and gallium.** Elemental distribution of Rb, In and Ga (top view) at four different positions of the bare ACIGS absorber film (after removal of the window and buffer layers via an HCl etch), as obtained from nano-XRF analysis. Thickness differences were again corrected by using the intensity variations in the respective Se maps. The colour code refers to the density (in  $\text{ng cm}^{-2}$ ), ranging from the corresponding minimum (Min) to the maximum (Max) values.

underneath the buffer layer, while GDOES also reveals an agglomeration at the back contact (that is, between  $\text{MoSe}_2$  and ACIGS), in line with the nano-XRF results. The Na concentration (Na added as a NaF precursor) in the absorber is below the GDOES detection limit, but it can be found in the Mo layer. At this stage, we do not understand why the Na content in the ACIGS bulk is exceptionally low, since typically the sensitivity provided by the GDOES method is sufficient to distinguish the Na signal from the measurement noise. Furthermore, it is not clear to what extent Na is present at the ACIGS/ $\text{MoSe}_2$  interface and in GBs, from where it was found to be pushed out by the heavier Rb in prior works<sup>46–48</sup>. In earlier studies, a Na peak was found at the (A)CIGS surface in GDOES, due to the Na accumulation in ordered vacancy compounds (OVCs)<sup>49,50</sup>. Rubidium was found to not (entirely) replace Na in these OVCs<sup>49</sup>. This Na peak is absent in our measurement, and thus, we assume that the ACIGS film of our record device exhibits only a very minor amount of surface OVC patches, despite its relatively low  $[\text{I}]/[\text{III}]$  of 0.84.

### Microscopic characterization of the heterojunction region

We analysed one of the Rb-rich patches found at the absorber surface in Fig. 5 in more detail ('Pos2.2') (Fig. 6). The elemental maps of the corresponding heterojunction region, obtained from STEM-EDS, are shown in Fig. 6a. It is evident that the Rb-rich area is depleted in Cu, in Ga and locally also in Ag. The quantified elemental concentrations inside and outside the Rb-rich patch (positions 1 and 2 in Fig. 6b) are shown in Fig. 6d. Relatively, the Cu and Ga contents are most reduced in the patch, where Rb reaches about 8 at.%. Considering that the lamella is  $>60$  nm thick, it is likely that the Rb-rich phase changes its lateral extension throughout the depth of the lamella. As a result, the volume analysed by EDS may contain a mixture of the ACIGS chalcopyrite phase and the Rb-rich patch, leading to an apparent concentration that is 'artificially' too low in Rb and too high in Cu and Ga. This is further highlighted by the inhomogeneous Rb concentration measured in the patch, as seen in Fig. 6c (highest local Rb concentration is 12 at.%). Thus, we speculate that the Rb-rich regions, frequently found at the CdS/absorber interface, are  $\text{RbInSe}_2$ , or another Rb–In–Se compound. However, we cannot exclude that this phase still contains some amount of Cu, Ga and Ag. Figure 6e,f shows higher-magnified BF- and dark field (DF)-STEM images of the patch. An abrupt change in lattice structure from the chalcopyrite to

the Rb–In–Se phase is evident. A layered structure of atomic rows is identified inside the Rb-rich patch, as reported in earlier studies and attributed to the  $\text{RbInSe}_2$  compound formation (monoclinic system, space group  $\text{C2/c}$ )<sup>51–53</sup>. It is unclear what kind of impact those Rb–In–Se patches have on the device performance. However, it is deemed unlikely that they have a beneficial effect, since they are rather widely dispersed and separated. In case the patches are indeed  $\text{RbInSe}_2$ , a possible parasitic absorption would not be very detrimental though, due to its small extension and large bandgap of 2.8 eV (ref. 54).

We could not detect the Rb-rich phase via sheer phase contrast in (S)TEM alongside the CdS/absorber interface at positions outside those Rb-rich patches (see typical STEM images in Supplementary Fig. 7). Still, as we found via nano-XRF, rubidium seems to be present everywhere underneath the CdS.

To reveal chemical changes across the heterojunction, a STEM-EDS line scan was extracted along the black dashed arrow in Fig. 6a. The normalized elemental profiles are shown in Supplementary Fig. 8. The Rb agglomeration at the ACIGS/CdS interface is evident. Interestingly, the Cu and Ga signals drop about 5 nm before the other absorber elements. This is in line with the formation of a very thin (Ag,Rb)–In–Se compound (potentially  $(\text{Ag,Rb})\text{InSe}_2$ ) at the absorber surface. We performed a similar analysis for 'Pos1.2' on lamella 1. The results are shown in Supplementary Figs. 9 and 10. Again, we found Rb agglomeration at the interface and the Cu and Ga signals drop before (here -3 nm) the ones of In and Se. However, at this position the Ag also drops with the Cu and Ga signals. In all cases, the relative Ag signal is still quite high in the CdS film. This is probably caused by an artefact of the lamella preparation via the FIB, which triggers diffusion of mobile Ag atoms during thermal stress (or maybe even during e-beam exposure). Summarizing all findings, we speculate that a very thin ( $<5$  nm)  $\text{RbInSe}_2$  phase forms everywhere alongside the CdS/ACIGS interface between the  $\text{RbInSe}_2$  patches.

Another feature observed in Supplementary Figs. 8 and 10 is the slight in-diffusion of Cd (depth -1–2 nm) into the thin  $\text{RbInSe}_2$  layer (see differences in Cd and S signals). An interdiffusion of Cd and Cu has been observed before at CIGS/CdS interfaces<sup>55,56</sup>. Earlier studies suggest that the resulting creation of  $\text{Cd}_{\text{Cu}}$  donor defects in the chalcopyrite (or OVC) lattice leads to the formation of a beneficial buried homojunction and a strong type inversion at the CdS/absorber interface<sup>56–58</sup>. However, these prior investigations did not consider or study the effect of Cd incorporation into the potential  $\text{RbInSe}_2$  surface phase that probably has a completely different impact. Furthermore, we cannot exclude that Cd diffuses into the absorber only during the lamella preparation (similarly to a possible Ag smear-out).

### Characterization of the back region and GBs

Finally, we address the chemical variations in the back-contact region and at ACIGS GBs. Figure 7 shows the elemental distributions in the vicinity of the Mo layer at 'Pos1.4' (lamella 1), as measured by STEM-EDS. Two more EDS mappings were conducted close to the Mo electrode at 'Pos2.3' and 'Pos1.3', which are shown in Supplementary Figs. 11 and 12, respectively. The results are very similar to the ones shown in Fig. 7.

First, we found abrupt strong changes in Ga and In (that is, in GGI) from one grain to another, as was reported in earlier studies for the bottom part of chalcopyrite absorbers<sup>59</sup>. We detected again rubidium in most GBs, while it seems to be absent in one GB in Fig. 7 (in agreement with the corresponding nano-XRF in Fig. 3). Most of the investigated GBs are depleted in Cu, but enriched in Ag. Some GBs are further depleted in In and enriched in Ga, as can be clearly seen in Supplementary Fig. 11 and also for a GB close to the heterojunction in Supplementary Fig. 9. Overall, the Cu depletion is more or less balanced by the Ag enrichment, so that the  $[\text{I}]/[\text{III}]$  ratio does not change notably across the GBs (see, for example,  $[\text{I}]/[\text{III}]$  map in Supplementary Fig. 9). Atom probe tomography (APT) characterizations of GBs in ACIGS absorbers with similar AAC of 0.2 (but KF- instead of RbF-PDT) reported in earlier studies showed clear reduction in Cu, increase in In (slightly in Se) and no notable change in

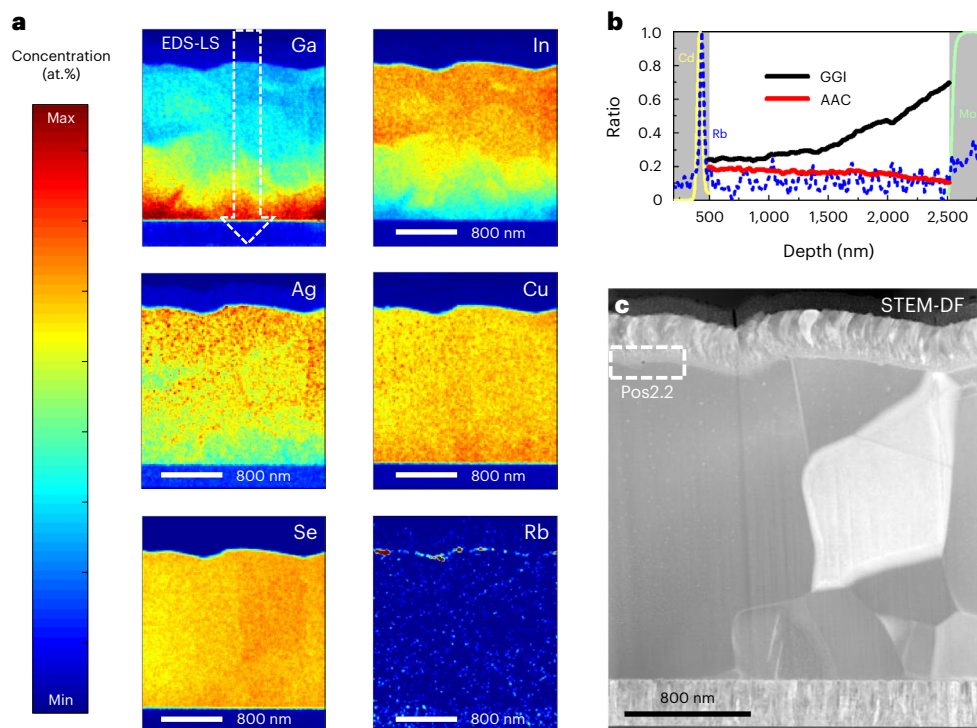


**Fig. 5 | STEM-EDS analysis of the complete solar cell.** **a**, Distributions of the absorber elements and Rb at 'Pos2.1' (lamella 2), as deduced by STEM-EDS. The colour code refers to the atomic concentrations in at.%, ranging from the corresponding minimum (Min) to the maximum (Max) values. **b**, GGI, AAC and normalized Cd, Mo and Rb depth profiles, extracted along the rectangle

indicated by the dashed white arrow in the Ga map in **a** (depth corresponds to direction of the arrow). The grey areas indicate the electrode/buffer regions. **c**, Corresponding STEM-DF image. The region 'Pos2.2', as indicated by the dashed white box, is shown in more detail in Fig. 6.

Ag and Ga (ref. 60). At this point, it is unclear why those prior studies led to partly different results. A possible reason why we found Ag-rich GBs in this study may be the diffusion of Ag into GBs during sample preparation. Yet, since APT sample preparation also requires FIB milling, the same effect would be expected in those prior APT studies. Moreover, STEM-EDS analysis of wide-gap ACIGS films reported in an earlier work showed Cu and Ag depletion in GBs<sup>49</sup>, which is in contrast to the findings shown in this work. A possible explanation is that only Ga-rich absorbers (that is, wide-gap) show Ag-depleted GBs and Ga-poor absorbers do not, similar to the Ag-Ga anti-correlation seen in the grain interior<sup>45</sup>. Indeed, we found the silver-enriched GBs in Fig. 7 (and Supplementary Fig. 11) only in regions of low Ga content, while GBs close to the back contact (high Ga concentration) do not show an Ag enrichment. More statistics are needed to draw further conclusions.

In prior publications it was proposed that Cu depletion at CIGS GBs often makes them benign (depends on oxygen and Na content) due to a favourable band bending<sup>61</sup>. In addition, the Rb decoration of GBs was claimed to exclusively lead to beneficial upward band bending at GBs<sup>62</sup>. Other studies conclude that the  $V_{oc}$  of state-of-the-art chalcopyrite devices is still limited by GB recombination, despite a substantially reduced recombination velocity via an RbF-PDT<sup>22</sup>. More sophisticated methods are needed to study the effect of GBs on the overall recombination rate in the champion solar cell discussed in this work.

For the sake of a complete description of the absorber interfaces, STEM-BF images of the Mo/MoSe<sub>2</sub>/ACIGS interface region are provided in Supplementary Fig. 13. A roughly 7-nm-thick MoSe<sub>2</sub> layer (hexagonal structure with *c* axis perpendicular to Mo film<sup>63</sup>) can be identified.

#### Strategies for chalcopyrite solar cells towards 25%

We presented the electro-optical, morphological and chemical properties of a 23.64%-efficient ACIGS device. We believe that research and

innovation will lift efficiencies of chalcopyrite solar cells even higher in the future. As discussed in 'Electro-optical characterization of the champion device' section, the most straight-forward and possibly easiest way to improve the performance is to reduce the parasitic absorption in the buffer and window layer. Further strategies for manufacturing (A)CIGS-based solar cells towards (and beyond) 25% efficiency are discussed in detail in Supplementary Note 1. This also includes a discussion of the effect of light soaking on the doping density and  $V_{oc}$  (illustrated in Supplementary Fig. 14).

#### Conclusions

We reveal the properties of a chalcopyrite-based solar cell with a certified efficiency of 23.6% (23.8% in-house measurement). The performance improvement is enabled by a high-concentration alloying of silver (AAC = 0.19) of the absorber film and the minimization of lateral and in-depth compositional fluctuations (that is,  $E_c$  fluctuations) at the absorber surface and in the SCR. Instead of a conventional 'notch' GGI profile, we implement a 'hockey stick'-like profile, with rather constant GGI in the upper half of the ACIGS film. We demonstrate that the RbF-PDT led to several absorber modifications. First, we show that the absorber surface is depleted in Cu and Ga (and locally Ag) and enriched in Rb. The results suggest the presence of a Rb-In-Se phase (probably RbInSe<sub>2</sub>) that is locally appearing in the form of larger patches (some >50 nm) and otherwise as a thin layer (<5 nm). We also found rubidium in certain (presumably random high-angle) GBs and at the back-contact interface. Most of the analysed GBs are depleted in Cu but enriched in Ag, while some also show Ga enrichment and In depletion. Further studies are needed to assess the role of GBs and its chemistry on the performance of the solar cell.

Avoiding parasitic absorption in the window and buffer layers, while maintaining the same  $V_{oc}$  and FF level, seems to be the most

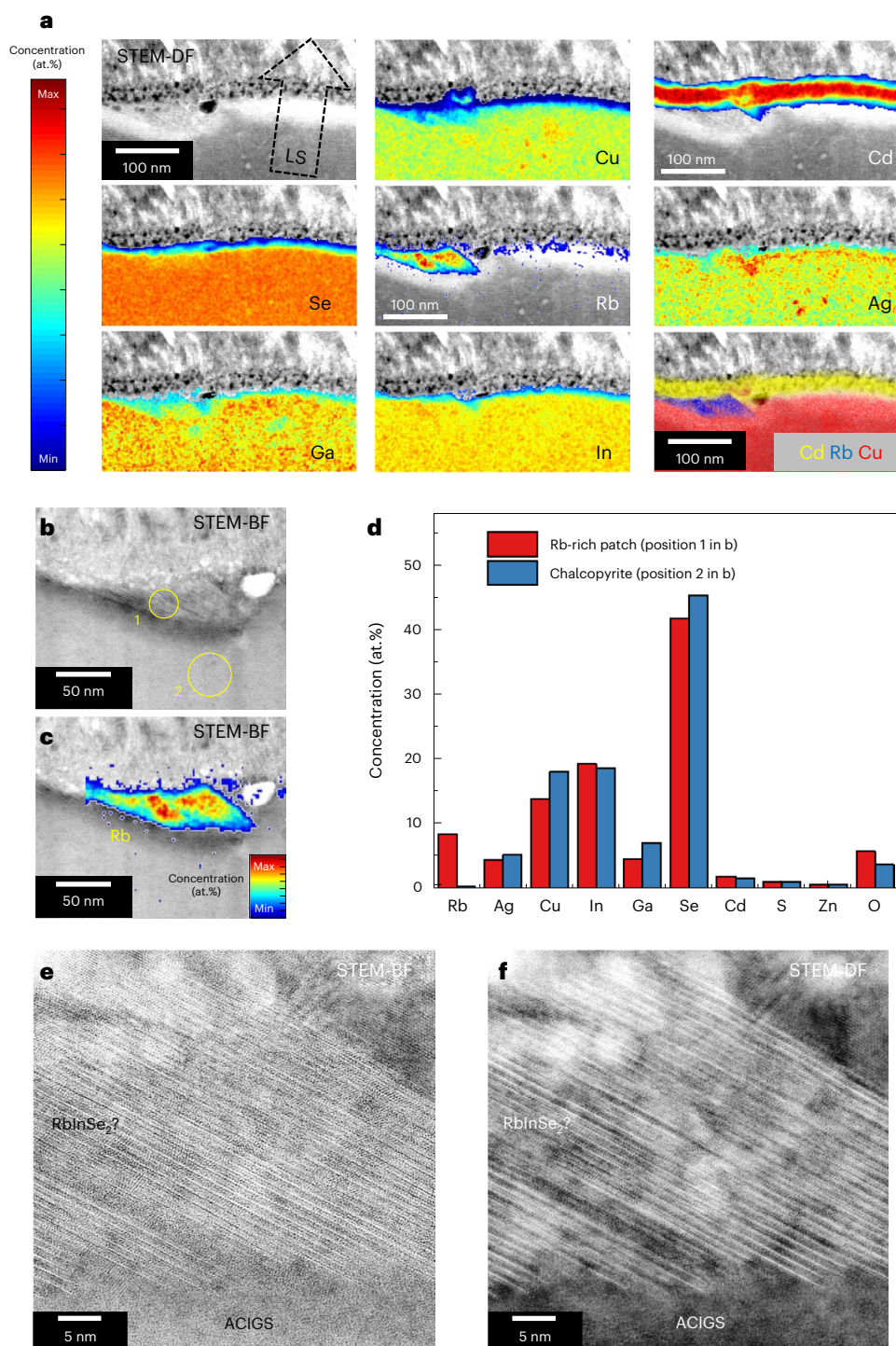


**Fig. 6 | STEM-EDS analysis of the absorber/buffer heterojunction. a**, Distributions of absorber elements, Rb and Cd at 'Pos2.2' (lamella 2, see position also in Fig. 5c), as deduced by STEM-EDS. The maps are superimposed onto the corresponding STEM-DF image, and the colour code refers to the atomic concentrations in at.%, ranging from the corresponding minimum (Min) to the maximum (Max) values. In addition, a combination of the Cd, Rb and Cu signals is shown (transparency of different colors scales with concentration, that is low

concentration has high transparency and vice versa). The black dashed arrow in the STEM-DF image indicates the position of an extracted EDS line scan, which is shown in detail in Supplementary Fig. 8. **b**, STEM-BF image of the Rb-rich patch identified in **a**. **c**, Same image with superimposed Rb concentration map from **a**. **d**, Quantified elemental concentrations, extracted from the circular regions 1 and 2 indicated in **b**. **e**, **f**, STEM-BF (**e**) and STEM-DF (**f**) images of the Rb-rich patch at higher magnification.

straight-forward approach to push the efficiency towards 25%. To go beyond this level, the absorber quality has to be further improved and ERE values much higher than 1.6% (reported in the present study) need to be realized to further reduce the  $V_{oc}$  deficit and the ideality factor ( $n = 1.3$  in the present work).

## Methods

### Solar cell processing

The champion solar cell discussed in this work has the following stack sequence: soda lime glass/Mo/NaF-precursor/ACIGS/RbF-PDT/CdS/i-ZnO/ZnO:Al/MgF<sub>2</sub>. First, a 290-nm-thick Mo back contact was



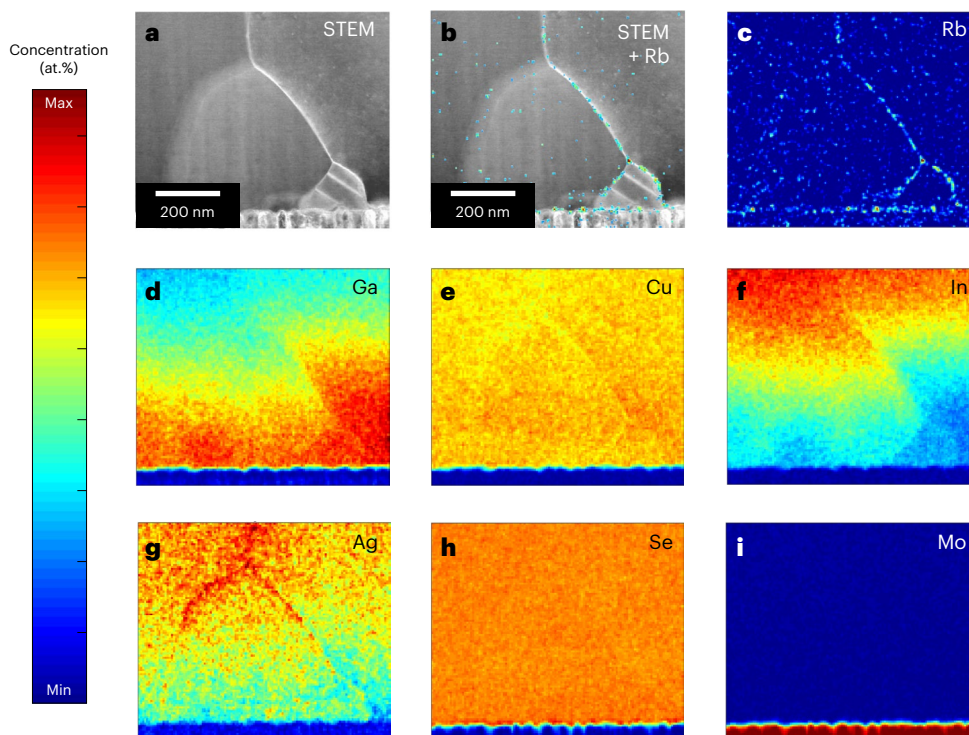


**Fig. 7 | STEM-EDS analysis of the back-contact region.** **a**, DF-STEM image of 'Pos1.4' (lamella 1). **b**, Semi-transparent rubidium concentration map, as deduced by STEM-EDS, superimposed on the STEM image. Pixels with Rb concentrations at the noise level are set fully transparent. The highest Rb concentration is found

at a triple junction. **c–i**, Distributions of elements close to the Mo back contact, as deduced by STEM-EDS. The color code of the elemental maps refers to the atomic concentrations in at.%, ranging from the corresponding minimum (Min) to the maximum (Max) values.

sputter-deposited (DC magnetron) and then coated with a 10-nm-thick NaF precursor layer by thermal evaporation. No alkali diffusion barrier was introduced underneath the back contact. A modified three-stage (I-poor → I-rich → I-poor) co-evaporation process was applied to grow 2.0–2.1- $\mu\text{m}$ -thick ACIGS films at a maximum substrate temperature of about 530 °C. All elements were provided in all three deposition phases. Further information about the sequence of the metal evaporation rates (ratios) can be obtained from an earlier work<sup>64</sup>. The final absorber composition was GGI of 0.28, AAC of 0.19 and [I]/[III] = 0.84, as measured by XRF. After ACIGS deposition a heavy alkali PDT was applied by depositing 3–5 nm of RbF at 350 °C without breaking the vacuum and without additional Se supply. Subsequently, a 25-nm-thick CdS buffer layer was grown via CBD at 60 °C. Finally, a 30- and 230-nm-thick i-ZnO and ZnO:Al layer was RF- and DC-sputtered on top, respectively.

Afterwards, 27 individual cells with an area of 1.03 cm<sup>2</sup> were defined via a photolithography process and subsequent selective removal of the window layers by etching in acetic acid. On top of the transparent conductive oxide an aluminum grid with 12  $\mu\text{m}$  linewidth (1 mm pitch) and in contact with a busbar frame outside the active/aperture area of the cell was deposited via thermal evaporation. Finally, a 110-nm-thick MgF<sub>2</sub> ARC was deposited across the whole area. The majority (22) of the 27 cells have efficiencies  $\eta > 23\%$ , very close to the cell discussed in this article that was certified by Fraunhofer ISE, and the corresponding JV parameters, as well as all JV curves, can be found in Supplementary Fig. 15 and Supplementary Table 1.

### Electro-optical characterization of solar cells

All JV and EQE measurements were conducted after light soaking the complete cells for 24 h (no active cooling, that is cell temperature about 50 °C). In case of the in-house JV measurement (red crosses in Fig. 1a), the entire solar cell, with an area of 1.03 cm<sup>2</sup>, was illuminated. For the certified measurement done by Fraunhofer ISE in Germany (black line

in Fig. 1a), a shadow mask with an aperture area of 0.90 cm<sup>2</sup> was used. The JV data of the in-house measurement were fitted using a one-diode model, by numerically solving the Shockley equation:

$$J = J_0 \times \left( \exp\left(\frac{e(V - JR_S)}{nkT}\right) - 1 \right) + \frac{V - JR_S}{R_{p,app}} - J_{SC} \quad (2)$$

at each voltage value and globally minimizing the deviation of the results from the measured current densities  $J$ . The in-house JV and EQE measurements were performed at  $T = 25$  °C using an ABET Technologies 'Sun 3000 Solar Simulator' (Xenon lamp) and a Bentham 'PVE 300' tool, respectively. For the EQE measurement the complete cell was illuminated with monochromatic light, so shading losses by the grid area are included in the corresponding spectrum (same for certified ISE measurement). The PL measurements were conducted in a setup consisting of a FSL1000 photoluminescence spectrophotometer from Edinburgh instruments equipped with an integrating sphere (coated with BaSO<sub>4</sub>) and a nitrogen cooled (−80 °C) photomultiplier tube as a detector. The sample was excited by a 520 nm continuous wave laser at an intensity of about 1 sun (number of photons in laser beam matches the number of photons absorbed by the sample under illumination with the AM1.5G spectrum). The settings were chosen as 0.4 nm emission band width, 0.5 s dwell time and 1 nm step size. For the ERE measurement the emission band width was increased to 1 nm, the dwell time kept at 0.5 s and the step size was 1 nm for the emission range but 0.1 nm for the scatter range, to fully resolve the laser peak. First, the sample's emission ( $\lambda = 850$ – $1,300$  nm) and reflection in the laser wavelength region ( $\lambda = 515$ – $535$  nm) was measured. Then, a BaSO<sub>4</sub> plug was inserted instead of the sample to obtain the background in the emission range and the reference signal in the scattering range. In this way the absorption and emission (in number of photons) were obtained after integration, and the ERE was calculated by  $\text{ERE} = (E_{m_A} - E_{m_B})/$

( $\text{Scat}_B - \text{Scat}_A$ ), Em stands for the integrated yield in the emission range and Scat for the yield in the scattering range. Subscript A is for the sample and B is for the  $\text{BaSO}_4$  reference. To get the ERE value of 1.6%, the integration was done between  $\lambda = 520\text{--}529$  nm for the scattering range and  $\lambda = 1,000\text{--}1,280$  nm for the emission range (see spectra in Supplementary Fig. 3).

Capacitance–voltage profiling was conducted from  $V = -0.56$  to  $+0.6$  V at 60 kHz and an amplitude of 25 mV, using an Agilent 4284A precision LCR meter and a Keithley 2401 source meter. A dielectric constant of  $\epsilon_r = 10$  was assumed for the ACIGS material.

### Material characterization

The integral ACIGS absorber composition was determined with a Helmut Fischer XRF, using a ‘Fischerscope X-ray 5400’ head. A Zeiss Merlin SEM (acceleration voltage of 5 kV) was used to investigate the solar cell cross-sections and absorber surface after removal of the window and buffer layers via an HCl etch. STEM and EDS analyses were performed on a FEI Titan Themis XFEI instrument equipped with a Super-X detector and operated at 200 kV. The TEM lamellae were prepared via FIB in a Crossbeam 550 ZEISS system, following the lift-out technique. A final milling step at maximum 2 kV ion accelerating voltage was performed on both sides of the lamellae, and no further electron exposure was done in the FIB before the TEM analyses. The local composition of the ACIGS samples was further measured via nano-XRF at the NanoMAX beamline of the MAXIV synchrotron radiation facility in Lund (Sweden)<sup>65</sup>. An X-ray energy of 16 keV with an average photon flux of  $8 \times 10^9$  photons  $\text{s}^{-1}$  and a spot size of  $55 \text{ nm} \times 55 \text{ nm}$  was employed for the measurements and a piezo stage was used to move the sample with a 55 nm step size and a counting time of 1,000 ms per pixel. The photon energy of 16 keV allowed to measure fluorescent photons corresponding to the K edges for Rb, Cu, Ga and Se and L edges for Ag, In and Ga. The X-ray signal was recorded using a RaySpec single element SSD detector. The area densities (in  $\text{ng cm}^{-2}$ ) of elements was estimated by fitting the XRF signal using the PyMca software<sup>66</sup>. Laterally integrated elemental depth profiles (analysed area  $\sim 3 \text{ mm}^2$ ) were deduced from a GDOES measurement in a Spectruma Analytik GDA 750HR system.

### Reporting summary

Further information on research design is available in the Nature Portfolio Reporting Summary linked to this article.

### Data availability

All data generated or analysed during this study are included in the published article and its Supplementary Information. Specific raw datasets are available from the corresponding author upon reasonable request.

### References

- Chirila, A. et al. Potassium-induced surface modification of  $\text{Cu}(\text{In,Ga})\text{Se}_2$  thin films for high-efficiency solar cells. *Nat. Mater.* **12**, 1107–1111 (2013).
- Nakamura, M. et al. Cd-free  $\text{Cu}(\text{In,Ga})(\text{Se,S})_2$  thin-film solar cell with record efficiency of 23.35%. *IEEE J. Photovolt.* **9**, 1863–1867 (2019).
- Jackson, P. et al. Effects of heavy alkali elements in  $\text{Cu}(\text{In,Ga})\text{Se}_2$  solar cells with efficiencies up to 22.6%. *Phys. Status Solidi RRL* **586**, 583–586 (2016).
- Kato, T., Wu, J., Hirai, Y., Sugimoto, H. & Bermudez, V. Record efficiency for thin-film polycrystalline solar cells up to 22.9% achieved by Cs-treated  $\text{Cu}(\text{In,Ga})(\text{Se,S})_2$ . *IEEE J. Photovolt.* **9**, 325–330 (2019).
- Hanket, G. M., Boyle, J. H. & Shafarman, W. N. Characterization and device performance of  $(\text{AgCu})(\text{In,Ga})\text{Se}_2$  absorber layers. In *34th IEEE Photovolt. Spec. Conf.* 001240–001245 (IEEE, 2009).
- Soltanmohammad, S., Tong, H. M., Anderson, T. J. & Shafarman, W. N. Reaction rate enhancement for  $\text{Cu}(\text{In,Ga})\text{Se}_2$  absorber materials using Ag-alloying. *IEEE J. Photovolt.* **9**, 898–905 (2019).
- Chen, L., Lee, J. & Shafarman, W. N. The comparison of  $(\text{Ag,Cu})(\text{In,Ga})\text{Se}_2$  and  $\text{Cu}(\text{In,Ga})\text{Se}_2$  thin films deposited by three-stage coevaporation. *IEEE J. Photovolt.* **4**, 447–451 (2014).
- Kim, G. et al. Thin Ag precursor layer-assisted co-evaporation process for low-temperature growth of  $\text{Cu}(\text{In,Ga})\text{Se}_2$  thin film. *ACS Appl. Mater. Interfaces* **11**, 31923–31933 (2019).
- Erslev, P. T., Lee, J., Hanket, G. M., Shafarman, W. N. & Cohen, J. D. The electronic structure of  $\text{Cu}(\text{In}_{1-x}\text{Ga}_x)\text{Se}_2$  alloyed with silver. *Thin Solid Films* **519**, 7296–7299 (2011).
- Keller, J. et al. Wide-gap  $(\text{Ag,Cu})(\text{In,Ga})\text{Se}_2$  solar cells with different buffer materials—a path to a better heterojunction. *Prog. Photovolt. Res. Appl.* **28**, 237–250 (2020).
- Chen, S., Gong, X. G. & Wei, S. H. Band-structure anomalies of the chalcopyrite semiconductors  $\text{CuGaX}_2$  versus  $\text{AgGaX}_2$  ( $X = \text{S}$  and  $\text{Se}$ ) and their alloys. *Phys. Rev. B* **75**, 205209 (2007).
- Huang, D. et al. General rules of the sub-band gaps in group-IV (Si, Ge, and Sn)-doped I-III-V<sub>2</sub>-type chalcopyrite compounds for intermediate band solar cell: a first-principles study. *Mater. Sci. Eng. B* **236–237**, 147–152 (2018).
- Sugimoto, H., Tomita, H., Yamaguchi, K., Hirai, Y. & Kato, T. High-performance near-stoichiometric  $\text{Cu}(\text{In,Ga})\text{Se}_2$  solar cells by sub-percent Ag-doping. In *29th PVSEC Conference* 723–726 (PVSEC, 2019).
- Green, M. A. Do built-in fields improve solar cell performance? *Prog. Photovolt. Res. Appl.* **17**, 57–66 (2009).
- Kobayashi, T. et al. Impacts of surface sulfurization on  $\text{Cu}(\text{In}_{1-x}\text{Ga}_x)\text{Se}_2$  thin-film solar cells. *Prog. Photovolt. Res. Appl.* **23**, 1367–1374 (2015).
- Avancini, E. et al. Impact of compositional grading and overall Cu deficiency on the near-infrared response in  $\text{Cu}(\text{In,Ga})\text{Se}_2$  solar cells. *Prog. Photovolt. Res. Appl.* **25**, 233–241 (2017).
- Reinhard, P. et al. Flexible  $\text{Cu}(\text{In,Ga})\text{Se}_2$  solar cells with reduced absorber thickness. *Prog. Photovolt. Res. Appl.* **23**, 281–289 (2015).
- Gong, J. et al. Enhancing photocurrent of  $\text{Cu}(\text{In,Ga})\text{Se}_2$  solar cells with actively controlled Ga grading in the absorber layer. *Nano Energy* **62**, 205–211 (2019).
- Friedlmeier, T. M. et al. Improved photocurrent in  $\text{Cu}(\text{In,Ga})\text{Se}_2$  solar cells: from 20.8% to 21.7% efficiency with CdS buffer and 21.0% Cd-free. *IEEE J. Photovolt.* **5**, 1487–1491 (2015).
- Chirilă, A. et al. Highly efficient  $\text{Cu}(\text{In,Ga})\text{Se}_2$  solar cells grown on flexible polymer films. *Nat. Mater.* **10**, 857–861 (2011).
- Werner, J. H., Mattheis, J. & Rau, U. Efficiency limitations of polycrystalline thin film solar cells: case of  $\text{Cu}(\text{In,Ga})\text{Se}_2$ . *Thin Solid Films* **480–481**, 399–409 (2005).
- Krause, M. et al. Microscopic origins of performance losses in highly efficient  $\text{Cu}(\text{In,Ga})\text{Se}_2$  thin-film solar cells. *Nat. Commun.* **11**, 4189 (2020).
- Carron, R. et al. Heat–light soaking treatments for high-performance CIGS solar cells on flexible substrates. Preprint at *Research Square* <https://doi.org/10.21203/rs.3.rs-2116168/v1> (2022).
- Khatri, I., Shudo, K., Matsuura, J., Sugiyama, M. & Nakada, T. Impact of heat–light soaking on potassium fluoride treated CIGS solar cells with CdS buffer layer. *Prog. Photovolt. Res. Appl.* **26**, 171–178 (2018).
- Scheer, R. Activation energy of heterojunction diode currents in the limit of interface recombination. *J. Appl. Phys.* **105**, 104505 (2009).
- Nadenau, V., Rau, U., Jasenek, A. & Schock, H. W. Electronic properties of  $\text{CuGaSe}_2$ -based heterojunction solar cells. Part I. Transport. *Anal. J. Appl. Phys.* **87**, 584–593 (2000).
- Keller, J., Lindahl, J., Edoff, M., Stolt, L. & Törndahl, T. Potential gain in photocurrent generation for  $\text{Cu}(\text{In,Ga})\text{Se}_2$  solar cells by using  $\text{In}_2\text{O}_3$  as a transparent conductive oxide layer. *Prog. Photovolt. Res. Appl.* **24**, 102–107 (2016).

28. Keller, J., Stolt, L., Edoff, M. & Törndahl, T. Atomic layer deposition of  $\text{In}_2\text{O}_3$  transparent conductive oxide layers for application in  $\text{Cu}(\text{In,Ga})\text{Se}_2$  solar cells with different buffer layers. *Phys. Status Solidi A* **213**, 1541–152 (2016).
29. Chantana, J., Kawano, Y., Nishimura, T., Mavlonov, A. & Minemoto, T. Impact of Urbach energy on open-circuit voltage deficit of thin-film solar cells. *Sol. Energy Mater. Sol. Cells* **210**, 110502 (2020).
30. Carron, R. et al. Advanced alkali treatments for high-efficiency  $\text{Cu}(\text{In,Ga})\text{Se}_2$  solar cells on flexible substrates. *Adv. Energy Mater.* **9**, 1900408 (2019).
31. Siebentritt, S. et al. Heavy alkali treatment of  $\text{Cu}(\text{In,Ga})\text{Se}_2$  solar cells: surface versus bulk effects. *Adv. Energy Mater.* **10**, 1903752 (2020).
32. Ugur, E. et al. Life on the Urbach edge. *J. Phys. Chem. Lett.* **13**, 7702–7711 (2022).
33. Shockley, W. & Queisser, H. J. Detailed balance limit of efficiency of p–n junction solar cells. *J. Appl. Phys.* **32**, 510–519 (1961).
34. Siebentritt, S. et al. How photoluminescence can predict the efficiency of solar cells. *J. Phys. Mater.* **4**, 042010 (2021).
35. Siebentritt, S. et al. Photoluminescence assessment of materials for solar cell absorbers. *Faraday Discuss.* **239**, 112–129 (2022).
36. Green, M. A. & Ho-Baillie, A. W. Y. Pushing to the limit: radiative efficiencies of recent mainstream and emerging solar cells. *ACS Energy Lett.* **4**, 1639–1644 (2019).
37. Green, M. A. et al. Solar cell efficiency tables (Version 61). *Prog. Photovolt. Res. Appl.* **31**, 3–16 (2023).
38. Schöppe, P. et al. Overall distribution of rubidium in highly efficient  $\text{Cu}(\text{In,Ga})\text{Se}_2$  solar cells. *ACS Appl. Mater. Interfaces* **10**, 40592–40598 (2018).
39. Schöppe, P. et al. Revealing the origin of the beneficial effect of cesium in highly efficient  $\text{Cu}(\text{In,Ga})\text{Se}_2$  solar cells. *Nano Energy* **71**, 104622 (2020).
40. Schöppe, P. et al. Rubidium segregation at random grain boundaries in  $\text{Cu}(\text{In,Ga})\text{Se}_2$  absorbers. *Nano Energy* **42**, 307–313 (2017).
41. Siebentritt, S. & Weiss, T. P. Chalcopyrite solar cells—state-of-the-art and options for improvement. *Sci. China Phys. Mech. Astron.* **66**, 217301 (2023).
42. Reinhard, P. et al. Alkali-templated surface nanopatterning of chalcogenide thin films: a novel approach toward solar cells with enhanced efficiency. *Nano Lett.* **15**, 3334–3340 (2015).
43. Keller, J. et al. Effect of KF absorber treatment on the functionality of different transparent conductive oxide layers in CIGSe solar cells. *Prog. Photovolt. Res. Appl.* **26**, 13–23 (2018).
44. Larsson, F., Donzel-Gargand, O., Keller, J., Edoff, M. & Törndahl, T. Atomic layer deposition of  $\text{Zn}(\text{O,S})$  buffer layers for  $\text{Cu}(\text{In,Ga})\text{Se}_2$  solar cells with KF post-deposition treatment. *Sol. Energy Mater. Sol. Cells* **183**, 8–15 (2018).
45. Sopiha, K. V. et al. Thermodynamic stability, phase separation and Ag grading in  $(\text{Ag,Cu})(\text{In,Ga})\text{Se}_2$  solar absorbers. *J. Mater. Chem. A* **8**, 8740–8751 (2020).
46. Pianezzi, F. et al. Unveiling the effects of post-deposition treatment with different alkaline elements on the electronic properties of CIGS thin film solar cells. *Phys. Chem. Chem. Phys.* **16**, 8843–8851 (2014).
47. Raghuvanshi, M. et al. Influence of RbF post deposition treatment on heterojunction and grain boundaries in high efficient (21.1%)  $\text{Cu}(\text{In,Ga})\text{Se}_2$  solar cells. *Nano Energy* **60**, 103–110 (2019).
48. Vilalta-Clemente, A. et al. Rubidium distribution at atomic scale in high efficient  $\text{Cu}(\text{In,Ga})\text{Se}_2$  thin-film solar cells. *Appl. Phys. Lett.* **112**, 103105 (2018).
49. Keller, J., Aboulfadl, H., Stolt, L., Donzel-Gargand, O. & Edoff, M. Rubidium fluoride absorber treatment for wide-gap  $(\text{Ag,Cu})(\text{In,Ga})\text{Se}_2$  solar cells. *Sol. RRL* **6**, 2200044 (2022).
50. Keller, J. et al. On the paramount role of absorber stoichiometry in  $(\text{Ag,Cu})(\text{In,Ga})\text{Se}_2$  wide-gap solar cells. *Sol. RRL* **4**, 2000508 (2020).
51. Taguchi, N., Tanaka, S. & Ishizuka, S. Direct insights into  $\text{RbInSe}_2$  formation at  $\text{Cu}(\text{In,Ga})\text{Se}_2$  thin film surface with RbF postdeposition treatment. *Appl. Phys. Lett.* **113**, 113903 (2018).
52. Huang, F. Q., Deng, B., Ellis, D. E. & Ibers, J. A. Preparation, structures, and band gaps of  $\text{RbInS}_2$  and  $\text{RbInSe}_2$ . *J. Solid State Chem.* **178**, 2128–2132 (2005).
53. Weinberger, N. et al. Phase development in  $\text{RbInSe}_2$  thin films—a temperature series. *Scr. Mater.* **202**, 113999 (2021).
54. Kodalle, T. et al. Properties of co-evaporated  $\text{RbInSe}_2$  thin films. *Phys. Status Solidi RRL* **13**, 1800564 (2019).
55. Koprek, A. et al. Effect of Cd diffusion on the electrical properties of the  $\text{Cu}(\text{In,Ga})\text{Se}_2$  thin-film solar cell. *Sol. Energy Mater. Sol. Cells* **224**, 110989 (2021).
56. Nakada, T. & Kunioka, A. Direct evidence of Cd diffusion into  $\text{Cu}(\text{In,Ga})\text{Se}_2$  thin films during chemical-bath deposition process of CdS films. *Appl. Phys. Lett.* **74**, 2444–2446 (1999).
57. Migliorato, P., Shay, J. L., Kasper, H. M. & Wagner, S. Analysis of the electrical and luminescent properties of  $\text{CuInSe}_2$ . *J. Appl. Phys.* **46**, 1777–1782 (1975).
58. Ramanathan, K. et al. Advances in the CIS research at NREL. In *26th IEEE Photovolt. Spec. Conf.* 319–322 (IEEE, 1997).
59. Keller, J. et al. Grain boundary investigations on sulfurized  $\text{Cu}(\text{In,Ga})(\text{S,Se})_2$  solar cells using atom probe tomography. *Sol. Energy Mater. Sol. Cells* **117**, 592–598 (2013).
60. Aboulfadl, H. et al. Alkali dispersion in  $(\text{Ag,Cu})(\text{In,Ga})\text{Se}_2$  thin film solar cells—insight from theory and experiment. *ACS Appl. Mater. Interfaces* **13**, 7188–7199 (2021).
61. Raghuvanshi, M., Wuerz, R. & Cojocaru-Mirédin, O. Interconnection between trait, structure, and composition of grain boundaries in  $\text{Cu}(\text{In,Ga})\text{Se}_2$  thin-film solar cells. *Adv. Funct. Mater.* **30**, 2001046 (2020).
62. Nicoara, N. et al. Direct evidence for grain boundary passivation in  $\text{Cu}(\text{In,Ga})\text{Se}_2$  solar cells through alkali-fluoride post-deposition treatments. *Nat. Commun.* **10**, 3980 (2019).
63. Abou-Ras, D. et al. Formation and characterisation of  $\text{MoSe}_2$  for  $\text{Cu}(\text{In,Ga})\text{Se}_2$  based solar cells. *Thin Solid Films* **480–481**, 433–438 (2005).
64. Edoff, M. et al. High  $V_{\text{OC}}$  in  $(\text{Cu,Ag})(\text{In,Ga})\text{Se}_2$  solar cells. *IEEE J. Photovolt.* **7**, 1789–1794 (2017).
65. Johansson, U. et al. NanoMAX: the hard X-ray nanoprobe beamline at the MAX IV Laboratory. *J. Synchrotron Radiat.* **28**, 1935–1947 (2021).
66. Solé, V. A., Papillon, E., Cotte, M., Walter, P. & Susini, J. A multiplatform code for the analysis of energy-dispersive X-ray fluorescence spectra. *Spectrochim. Acta Part B* **62**, 63–68 (2007).

## Acknowledgements

This work was financially supported by the Swedish Energy Agency contracts P2020-90052 and P2021-90275 (SOLVE) (M.E.). We acknowledge MAX IV Laboratory for time on Beamline NanoMAX under Proposal 20220904 (N.M.M.). Research conducted at MAX IV, a Swedish national user facility, is supported by the Swedish Research council under contract 2018-07152, the Swedish Governmental Agency for Innovation Systems under contract 2018-04969, and Formas under contract 2019-02496. Support from S. Kalbfleisch at the beamline is highly acknowledged.

## Author contributions

J.K. conducted the SEM, CV, GDOES and most of the JV and EQE characterization, sent samples to external certification, and analyzed, processed and visualized all data, and wrote the paper. K.K. did the PLQY and PL measurements and performed, together

with N.M.M. and M.B., the nano-XRF analysis. N.M.M. further assisted in data analysis of the nano-XRF results. O.D.-G. did all the TEM and corresponding EDS characterization, as well as the sample preparation via the FIB technique. O.L., E.W., L.S. and M.E. developed the ACIGS process, manufactured the complete solar cell sample and did some of the JV and EQE characterization, as well as the in-house XRF measurement. M.E. supervised the work. All authors reviewed the paper.

## Funding

Open access funding provided by Uppsala University.

## Competing interests

O.L. is a co-founder and CTO of Evolar AB. E.W. is a co-founder and head of R&D at Evolar AB. Evolar AB is a company commercializing thin-film solar cells. The other authors declare no competing interests.

## Additional information

**Supplementary information** The online version contains supplementary material available at <https://doi.org/10.1038/s41560-024-01472-3>.

**Correspondence and requests for materials** should be addressed to Jan Keller.

**Peer review information** *Nature Energy* thanks the anonymous reviewers for their contribution to the peer review of this work.

**Reprints and permissions information** is available at [www.nature.com/reprints](http://www.nature.com/reprints).

**Publisher's note** Springer Nature remains neutral with regard to jurisdictional claims in published maps and institutional affiliations.

**Open Access** This article is licensed under a Creative Commons Attribution 4.0 International License, which permits use, sharing, adaptation, distribution and reproduction in any medium or format, as long as you give appropriate credit to the original author(s) and the source, provide a link to the Creative Commons licence, and indicate if changes were made. The images or other third party material in this article are included in the article's Creative Commons licence, unless indicated otherwise in a credit line to the material. If material is not included in the article's Creative Commons licence and your intended use is not permitted by statutory regulation or exceeds the permitted use, you will need to obtain permission directly from the copyright holder. To view a copy of this licence, visit <http://creativecommons.org/licenses/by/4.0/>.

© The Author(s) 2024

## Solar Cells Reporting Summary

Nature Portfolio wishes to improve the reproducibility of the work that we publish. This form is intended for publication with all accepted papers reporting the characterization of photovoltaic devices and provides structure for consistency and transparency in reporting. Some list items might not apply to an individual manuscript, but all fields must be completed for clarity.

For further information on Nature Research policies, including our [data availability policy](#), see [Authors & Referees](#).

### ► Experimental design

**Please check the following details are reported in the manuscript, and provide a brief description or explanation where applicable.**

#### 1. Dimensions

Area of the tested solar cells	<input checked="" type="checkbox"/> Yes <input type="checkbox"/> No	Certified measurement (Fraunhofer ISE): A = 0.89866 cm <sup>2</sup> (designated illumination area) In-house measurement: A = 1.03 cm <sup>2</sup> (total area) <i>Explain why this information is not reported/not relevant.</i>
Method used to determine the device area	<input checked="" type="checkbox"/> Yes <input type="checkbox"/> No	Certified measurement (Fraunhofer ISE): Aperture area of the mask (opening) In-house measurement: Determination of total cell area via camera. <i>Explain why this information is not reported/not relevant.</i>

#### 2. Current-voltage characterization

Current density-voltage (J-V) plots in both forward and backward direction	<input type="checkbox"/> Yes <input checked="" type="checkbox"/> No	Negligible hysteresis
Voltage scan conditions	<input type="checkbox"/> Yes <input checked="" type="checkbox"/> No	The measurement of the IV-curve is performed with a 4-quadrant power amplifier and a calibration resistor. The scan was performed in both directions. No difference was observed (no hysteresis). The final result is an average of both scan directions. The performance of the solar cell does not depend on the voltage scan conditions as long as they are in a reasonable range.
Test environment	<input type="checkbox"/> Yes <input checked="" type="checkbox"/> No	From Fraunhofer ISE certificate: The calibration of the test sample was performed at Standard Testing Conditions (STC) under irradiation with a steady-state class AAA solar simulator. The temperature of the solar cell is determined by a sensor and is adjusted to (25±0.5)°C. The irradiance is controlled with a monitor cell during the measurement in order to correct fluctuations linear. The divergence of the peripheral beams is < 8°. The solar cell is kept at a constant temperature on a vacuum chuck. State-of-the-art ACIGS solar cells are stable in air. Thus, we did not emphasize on the detailed test environment, like humidity level and so on.
Protocol for preconditioning of the device before its characterization	<input checked="" type="checkbox"/> Yes <input type="checkbox"/> No	Prior to the measurement the solar cell was illuminated (light-soaked, solar simulator, i.e. white light) for 24h without active cooling. <i>Explain why this information is not reported/not relevant.</i>
Stability of the J-V characteristic	<input checked="" type="checkbox"/> Yes <input type="checkbox"/> No	As mentioned in the manuscript, the efficiency increases during the first 24 hours of light-soaking (after keeping the sample in the dark) and then saturates. No decrease in efficiency was observed after longer exposure to light (up to several days were tested). The temporal stability of the solar cell performance was not controlled during the certification by Fraunhofer ISE. <i>Explain why this information is not reported/not relevant.</i>

#### 3. Hysteresis or any other unusual behaviour

Description of the unusual behaviour observed during the characterization	<input type="checkbox"/> Yes <input checked="" type="checkbox"/> No	<i>Provide a description of hysteresis or any other unusual behaviour observed during the characterization.</i> Hysteresis or other unusual behaviour not observed
---	--	---

Related experimental data	<input type="checkbox"/> Yes <input checked="" type="checkbox"/> No	<div style="border: 1px solid #ccc; padding: 2px; margin-bottom: 2px;"><i>Provide a description of the related experimental data.</i></div> <div style="border: 1px solid #ccc; padding: 2px;">Hysteresis or other unusual behaviour not observed</div>
4. Efficiency		
External quantum efficiency (EQE) or incident photons to current efficiency (IPCE)	<input checked="" type="checkbox"/> Yes <input type="checkbox"/> No	<div style="border: 1px solid #ccc; padding: 2px;"> <p>From the Fraunhofer ISE certificate: The absolute differential spectral responsivity is determined in a wavelength range from 300 nm to 1200 nm at a short circuit current bias. The measurement is done with laser-monochromator setup with the DSR method in a two-beam geometry, using the two irradiation beams simultaneously:</p> <p>a) A stationary bias irradiation with irradiances EB (not measured explicitly). The variation of EB allows different short circuit currents ISC (EB),</p> <p>b) A time-modulated quasi-monochromatic measurement irradiation. The irradiance is determined by a primary calibrated reference solar cell (PTB).</p> <p>The operating point of the solar cell is defined by a bias current under short circuit conditions.</p> <p>Bias current : 0.3 mA, Nominal Value of the temperature of the object: 25 °C</p> <p>The voltage at the solar cell is set to below 0.03 VOC by a current-voltage-converter. The frequency of the chopped quasi-monochromatic measurement light is at 133 Hz. The spectral bandwidth (full width at half maximum) is below 5 nm. The temperature of the solar cell is determined by a sensor and adjusted to (25±0.5)°C.</p> </div> <div style="border: 1px solid #ccc; padding: 2px; margin-top: 2px;">The description in the manuscript is shorter to keep the Methods section concise.</div>
A comparison between the integrated response under the standard reference spectrum and the response measure under the simulator	<input type="checkbox"/> Yes <input checked="" type="checkbox"/> No	<div style="border: 1px solid #ccc; padding: 2px;"> <p>Certified Fraunhofer ISE:</p> <p><math>J_{sc,eqe} = 38.0 \text{ mA/cm}^2</math> from EQE (complete aperture area illuminated by monochromatic light)  <math>J_{sc,iv} = 38.3 \text{ mA/cm}^2</math> from IV</p> <p>In-house:</p> <p><math>J_{sc,eqe} = 38.3 \text{ mA/cm}^2</math> from EQE (complete cell illuminated by monochromatic light)  <math>J_{sc,iv} = 38.5 \text{ mA/cm}^2</math> from IV</p> </div> <div style="border: 1px solid #ccc; padding: 2px; margin-top: 2px;"><i>Explain why this information is not reported/not relevant.</i></div>
For tandem solar cells, the bias illumination and bias voltage used for each subcell	<input type="checkbox"/> Yes <input checked="" type="checkbox"/> No	<div style="border: 1px solid #ccc; padding: 2px; margin-bottom: 2px;"><i>Provide a description of the measurement conditions.</i></div> <div style="border: 1px solid #ccc; padding: 2px;">No tandem cell</div>
5. Calibration		
Light source and reference cell or sensor used for the characterization	<input type="checkbox"/> Yes <input checked="" type="checkbox"/> No	<div style="border: 1px solid #ccc; padding: 2px;"> <p>From Fraunhofer ISE certificate: The calibration of the test sample was performed at Standard Testing Conditions (STC) under irradiation with a steady-state class AAA solar simulator. The irradiance is controlled with a monitor cell during the measurement in order to correct fluctuations linear. The divergence of the peripheral beams is &lt; 8°.</p> <p>The solar cell is kept at a constant temperature on a vacuum chuck.</p> </div> <div style="border: 1px solid #ccc; padding: 2px; margin-top: 2px;">Too much information for Methods section. We wanted to keep it concise.</div>
Confirmation that the reference cell was calibrated and certified	<input type="checkbox"/> Yes <input checked="" type="checkbox"/> No	<div style="border: 1px solid #ccc; padding: 2px; margin-bottom: 2px;">Fraunhofer ISE (Germany)</div> <div style="border: 1px solid #ccc; padding: 2px;">Too much information for Methods section. We wanted to keep it concise.</div>
Calculation of spectral mismatch between the reference cell and the devices under test	<input type="checkbox"/> Yes <input checked="" type="checkbox"/> No	<div style="border: 1px solid #ccc; padding: 2px;"> <p>From Fraunhofer ISE certificate: The spectral mismatch - caused by the deviation of the class AAA simulator spectrum from the standard spectrum AM1.5G in combination with the difference between the spectral response of the reference cell and that of the device under test (DUT) – is calculated and corrected.</p> <p>For the spectral mismatch correction the spectral distribution of the solar simulator is measured with a spectroradiometer, the spectral response of the DUT is measured with a monochromator.</p> </div> <div style="border: 1px solid #ccc; padding: 2px; margin-top: 2px;">Too much information for Methods section. We wanted to keep it concise.</div>
6. Mask/aperture		
Size of the mask/aperture used during testing	<input checked="" type="checkbox"/> Yes <input type="checkbox"/> No	<div style="border: 1px solid #ccc; padding: 2px; margin-bottom: 2px;">Mask/aperture only used in certified measurements done at Fraunhofer ISE. Here, the size was <math>A = 0.9 \text{ cm}^2</math>.</div> <div style="border: 1px solid #ccc; padding: 2px;"><i>Explain why this information is not reported/not relevant.</i></div>

Variation of the measured short-circuit current density with the mask/aperture area

 Yes

 No

*Report the difference in the short-circuit current density values measured with the mask and aperture area.*

Only small variations observed

## 7. Performance certification

Identity of the independent certification laboratory that confirmed the photovoltaic performance

 Yes

 No

Fraunhofer ISE (Germany)

*Explain why this information is not reported/not relevant.*

A copy of any certificate(s)

 Yes

 No

*Certificate copies should be provided in the Supplementary information. Please state the supplementary item number.*

The certificates are available from the corresponding author upon reasonable request.

## 8. Statistics

Number of solar cells tested

 Yes

 No

This manuscript focuses on a single ACIGS solar cell that obtained the record efficiency. As mentioned in the text, 26 more solar cells (most of them also with efficiency > 23%) were prepared from the same ACIGS deposition run.

*Explain why this information is not reported/not relevant.*

Statistical analysis of the device performance

 Yes

 No

*State where this information can be found in the text.*

Since there is just a single cell discussed and presented, no statistical analysis was performed.

## 9. Long-term stability analysis

Type of analysis, bias conditions and environmental conditions

 Yes

 No

As mentioned in the manuscript, the efficiency increases during the first 24 hours of light-soaking (after keeping the sample in the dark) and then saturates. No decrease in efficiency was observed after longer exposure to light (up to several days were tested). Furthermore, the sample was stored for more than a year in a N<sub>2</sub>-cabinet and still reaches the same efficiency level (after light-soaking). No further stability tests (i.e. damp-heat, V-bias, etc) were done.

*Explain why this information is not reported/not relevant.*